Revision 1

Supplementary material

S1. Phase screening

Crystal	Ang. Range	N. of patterns	a (Å)	b (Å)	c (Å)	α (°)	β(°)	γ(°)
1 Pyrope	32°	67	11.4 11.439(2)	11.4	11.5	90.0 90	89.6 90	90.1 90
2 Forsterite	42°	88	4.76 4.753(1)	6.01 5.979(1)	10.1 10.196(1)	90.9 90	89.8 90	90.4 90
3 Magnesite	40°	83	4.62 4.6339(4)	4.59	15.0 15.0177(9)	89.7 90	90.1 90	120.3 120
4 11.5 Å	42°	88	8.89 9.012(1)	5.17 5.201(1)	? 23.202(5)	? 90	? 97.8(1)	90.4 90
5 Guaynaite	32°	67	2.92 2.955(1)	4.87 4.862(2)	4.30 4.298(2)	90.5 90	90.7 90	88.9 90

Table S1: Details of the fEDT data collections displayed in fig. 1 and the derived unit cell parameters compared with those from the literature (for pyrope Pavese et al. (1995), for forsterite Fisher & Medaris (1969), for magnesite Ross (1997), fot guyanaite Christensen et al. (1976)). The angular step between each pattern is 0.48° for each data collection

S2. Details of the structure solution and refinement of the new high pressure phases

11.5 Å phase

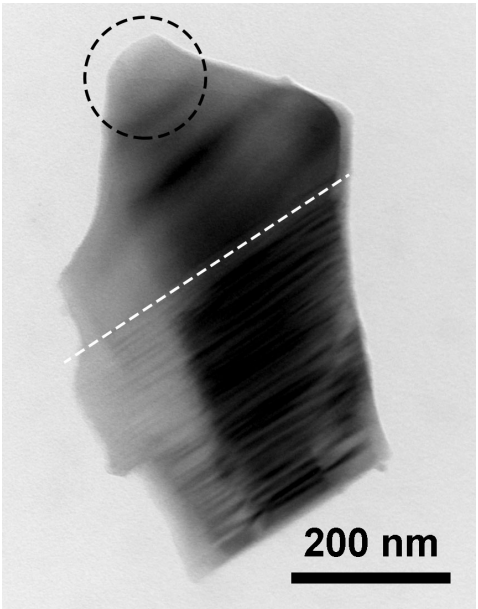

Figure S1 - Crystal grain of the 11.5 Å phase on which we collected the electron diffraction data for the structure solution. The crystal shows an area loaded with stacking defects (bottom) and an area in which the stacking is regular (top). A dashed line divides the two regions and a dashed circle indicates the zone on which the data collection has been performed. The circle has the same size as the electron beam.

Atom	X	y	z
Si1	0.9529(17)	0.103(4)	0.1212(6)
Al1	0.75	0.25	0
Mg1	0.090(2)	0.260(4)	-0.0015(9)
Mg2	0.301(2)	0.094(5)	0.1888(6)
Mg3	0.359(2)	0.100(5)	0.3119(6)
OH1	0.5	-0.029(8)	0.25
OH2	0.887(3)	0.402(6)	-0.0434(9)
OH3	0.297(2)	0.420(6)	0.2499(9)
OH4	0.219(3)	0.448(6)	-0.0456(9)
O1	0.097(3)	0.265(6)	0.1447(10)
O2	0.967(3)	-0.198(6)	0.1469(10)
O3	0.913(3)	0.102(6)	0.0493(9)
O4	0.813(3)	0.263(6)	0.1434(9)

Si1-O1	1.58(3)		Mg1-OH2	2.09(3)	
Si1-O2	1.67(4)		Mg1-OH2	2.04(4)	
Si1-O3	1.66(2)		Mg1-OH4	1.91(3)	
Si1-O4	1.65(3)	Ave: 1.64	Mg1-OH4	2.20(3)	
Al1-OH2 x2	1.87(3)		Mg1-O3	2.26(3)	
Al1-OH4 x2	1.89(3)		Mg1-O3	2.18(4)	Ave: 2.11
Al1-O3 x2	1.90(2)	Ave: 1.89			
Mg2-OH1	2.22(2)		Mg3-OH1	2.15(2)	
Mg2-OH3	2.21(4)		Mg3-OH3	2.22(3)	
Mg2-OH3	1.99(3)		Mg3-OH3	2.09(3)	
Mg2-O1	2.17(3)		Mg3-O1	2.03(4)	
Mg2-O2	2.18(3)		Mg3-O2	2.01(3)	
Mg2-O4	2.03(4)	Ave: 2.13	Mg3-O4	2.15(3)	Ave: 2.11

Table S2 – Atomic coordinates (top) and interatomic distances (bottom) of 11.5 Å phase after a kinematical crystal structure refinement against electron diffraction data. The thermal factor was kept fixed to 0.005 $Å^2$ and was not refined.

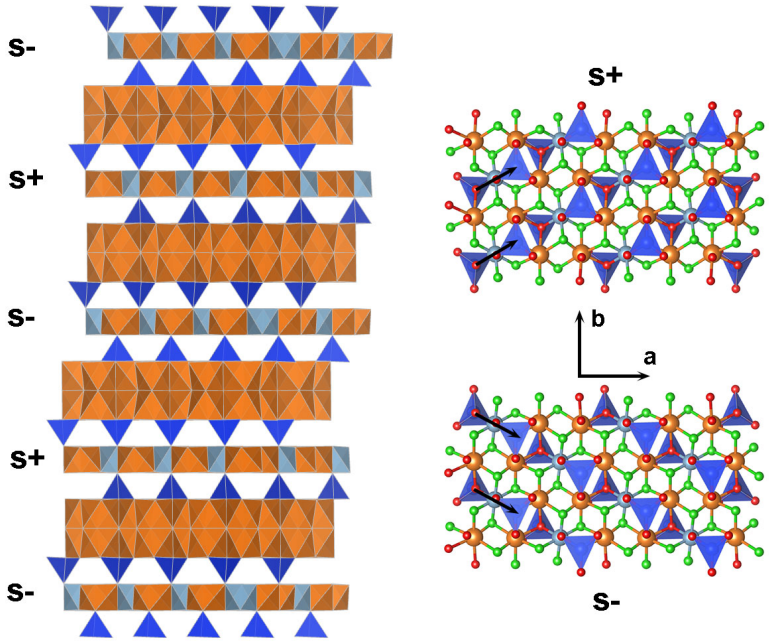

Figure S2. Right) the two different TOT modules of the 11.5 Å phase viewed along **c***. The two modules differ in the way the second T layer is shifted with respect to the first one. In the s+ module the shift is along [110] while in the s- module is along [1-10] instead. The shift vectors are displayed with arrows. Left) Stacking sequence of two unit cells along **c** of the 11.5 Å phase viewed along the [110] direction. In this projection the s+ and s- modules can be distinguished.

The HySo structure

Data set for the best (the one with minimum R value) structure solution:
Angular range: -60° to +50°
N. of patterns: 111, every 1°
Precession angle: 1°
N. of reflections (obs/all): 1245/2092
N. of independent reflections (obs/all): 495/698
R_{int} on I (obs/all) (%): 20.19/20.64
Coverage at 0.8Å : 71%
R_{sol}(SIR2011): 29%

Site	x	y	z
T1	0.702(7)	0.101(3)	-0.418(7)
M1	0	0	0.5
M2	0	0.106(2)	0
M3	0	0.218(7)	0.5
M4	0.5	0.318(4)	0
OH1	0.898(4)	0	0.128(3)
OH2	0.894(7)	0.207(1)	0.133(3)
O1	0.659(11)	0	-0.568(9)
O2	0.874(4)	0.108(3)	-0.359(4)
O3	0.634(4)	0.096(2)	-0.144(6)
O4	0.627(4)	0.180(3)	-0.621(9)
M5 (*)	0.5	0	0

Table S3: Atomic coordinates averaged from 7 different solutions obtained with direct methods on data sets collected on different crystals. The errors are estimated as standard deviation of the coordinates obtained with the different data sets. (*) The M5 position was detected only in 4 out of 7 data sets.

Site	Occupancy	x	y	z	Uiso ($Å^2$)
T1	1	0.6949(3)	0.10030(8)	-0.4228(3)	0.0047(4)
T2	0.203(7)	0.281(3)	0	-0.075(3)	0.025(5)
T3	0.209(6)	0.700(2)	0.1987(5)	0.0818(19)	0.027(3)
M1	1	0	0	0.5	0.0008(7)
M2	1	0	0.10530(14)	0	0.0093(5)
M3	1	0	0.21684(14)	0.5	0.0058(6)
M4	0.791(6)	0	0.31470(17)	0	0.0015(8)
M5	0.797(7)	0.5	0	0	0.0257(15)
OH1	1	0.8960(7)	0	0.1293(6)	0.0141(8)
OH2	1	0.8885(5)	0.20668(14)	0.1304(4)	0.0106(6)
O1	1	0.6573(6)	0	-0.5719(6)	0.0063(7)
O2	1	0.8766(4)	0.10621(14)	-0.3625(4)	0.0064(5)
O3	1	0.6293(4)	0.09715(15)	-0.1450(4)	0.0128(5)
O4	1	0.6298(5)	0.18083(14)	-0.6239(4)	0.0117(6)

T1-O2	1.653(5)							T3-O3	1.944(10)		
T1-O3	1.607(4)			T2-OH1	1.60(3)			T3-OH2	1.70(2)		
T1-O1	1.680(3)			T2-O3 x2	1.943(14)			T3-OH2	1.868(11)		
T1-O4	1.619(3)	ave	1.64	T2-O1	1.94(2)	ave	1.86	T3-O4	1.738(14)	ave	1.81
				M2-OH1 x2	1.984(5)			M3-O2 x2	2.146(4)		
M1-OH1 x2	1.984(4)			M2-O2 x2	2.011(3)			M3-OH2 x2	2.004(3)		
M1-O2 x4	2.109(3)	ave	2.07	M2-OH2 x2	1.970(4)	ave	1.99	M3-O4 x2	2.077(4)	ave	2.08
M4-O3 x2	1.968(4)										
M4-OH2 x2	2.050(4)			M5-O3 x4	2.065(4)						
M4-O4 x2	2.097(3)	ave	2.04	M5-O1 x2	2.422(4)	ave	2.18				

Table S4 – Atomic coordinates, site occupancies, thermal factors (top) and selected interatomic distances, of the HySo phase after dynamical structure refinement against electron diffraction data.

Calculation of the chemical formula of the defective HySo

The tetrahedral sites (T-sites), T2, T3 are too close to the M5 and M4 octahedra respectively, therefore they can be occupied only if the corresponding octahedron is empty. When one of these octahedral sites (O-sites) is empty (i.e. M5) we must suppose that both tetrahedra around it (i.e. two equivalent T2 sites) are occupied, as it happens with the Si_2O_7 groups which surrounds two empty octahedra, otherwise there will be a large hole in the structure with some oxygen atoms severely underbonded. A creation of a cluster of two tetrahedra and an octahedral vacancy in between (see figure S3) implies an increase of one atom per the cell. Furthermore since both Mg and Al in tetrahedral coordination are bonded only to oxygen, those anion sites that in the "ideal" structure are occupied by an OH group once bounded to a new tetrahedral site must become oxygen. There is only one of these sites per T2 and T3. In terms of charge balance the creation of the cluster implies an increase of the total charge of $2q_t$-q_v-2, where q_t is the oxidation state of the atoms going in the T-site, q_v is the oxidation state of the atom creating the vacancy in the O-site and the term -2 is due to the O-OH substitution. If for simplicity we consider that the same atom type that creates the vacancy occupies the new T-site, then if this atom is Al (q_t=q_v=+3), there is an increase in the charge by +1, while if it is Mg (q_t=q_v=+2) the charge is balanced. This means that in the case of Al T-sites, to balance the charge 1 Al in the O-layer must be substituted by 1 Mg, while the total number of Al in the structure does not change. In the case of Mg T-sites the charge is balanced, the number of Al in the structure is also unaltered and there is one Mg in excess in the T-sites. In conclusion independently from the type of atom that goes in the new T-sites the effect on the stoichiometry is an increase in the Mg content in the cell equal to half the fractional occupancy of the T sites multiplied by their multiplicity.

To obtain the final chemical formula as a function of the occupancy of the detected T2 and T3 sites we must take into account that the multiplicity of these sites is 4 and 8 respectively and that there are 4 formula units per cell. Then if x_{T2} x_{T3} are the occupancies of T2 and T3 respectively the chemical formula becomes: $(Mg_{3+0.5xT2+xT3}Al)(OH)_{3-xT2-2xT3}O_{xT2+2xT3}(Si_2O_7)$. In terms of moles of the oxides the formula becomes: $3+0.5x_{T2}+x_{T3}$ MgO + 0.5 Al2O3 + 2SiO2 $+(1.5 -0.5x_{T2}-x_{T3})$ H_2O so the formation of a defective structure involve a release of water and an incorporation of an equivalent number of moles of MgO, therefore the total number of oxygens in the cell is conserved and only Mg and H are exchanged.

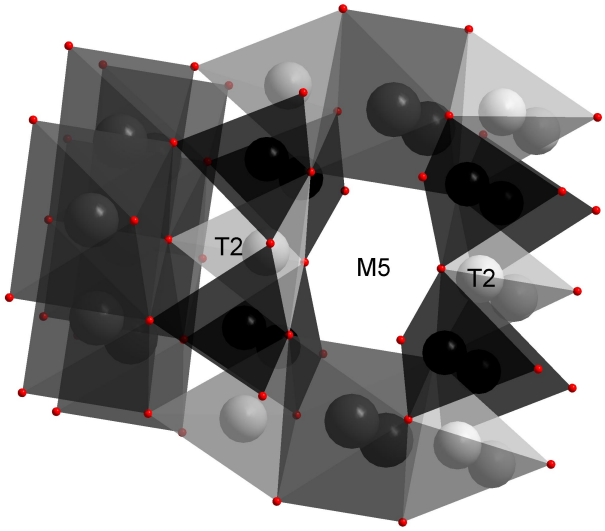

Figure S3: Cluster formed by two T2 occupied sites and the corresponding octahedral M5 site empty.

S3. Microprobe analysis

The mineral chemistry and BSE images were collected by electron microprobe using a JEOL JXA 8200 equipped with five WDS wavelength-dispersive spectrometers (Dipartimento di Scienze della Terra, Milano, Italy). Analyses were performed at 15 kV and 5 nA; natural and synthetic minerals were used as standards. All standards were calibrated within 0.5 % at one standard deviation. Raw data were corrected using a Phi–Rho–Z quantitative analysis program.
The chemical analysis of the 11.5 Å phase are reported in table S6. The results are plotted on a ternary compositional diagram (figure S4) and are consistent with a mixed analysis of 11.5 Å and HySo phase, as they plot on the join between the nominal stoichiometry of the two phases.

Analysis	JO1_1	JO1_2	JO1_3	JO1_4	JO1_5	JO1_6	JO1_7
SiO_2	27.35	25.06	23.79	26.06	26.33	26.11	28.22
Al_2O_3	12.06	11.62	11.93	11.02	11.24	11.23	11.42
MgO	46.96	46.13	43.46	47.00	47.69	47.51	46.66
Total	86.37	82.81	79.18	84.08	85.26	84.85	86.30
Recalculated on the basis of 9 cations and 15 oxygens							
Si	2.206	2.098	2.086	2.149	2.141	2.133	2.283
Al	1.147	1.146	1.233	1.071	1.077	1.081	1.089
Mg	5.646	5.755	5.680	5.777	5.781	5.786	5.628

Table S5 - Microprobe analysis of sample JO1 synthesized at at 6.5 GPa, 700°C

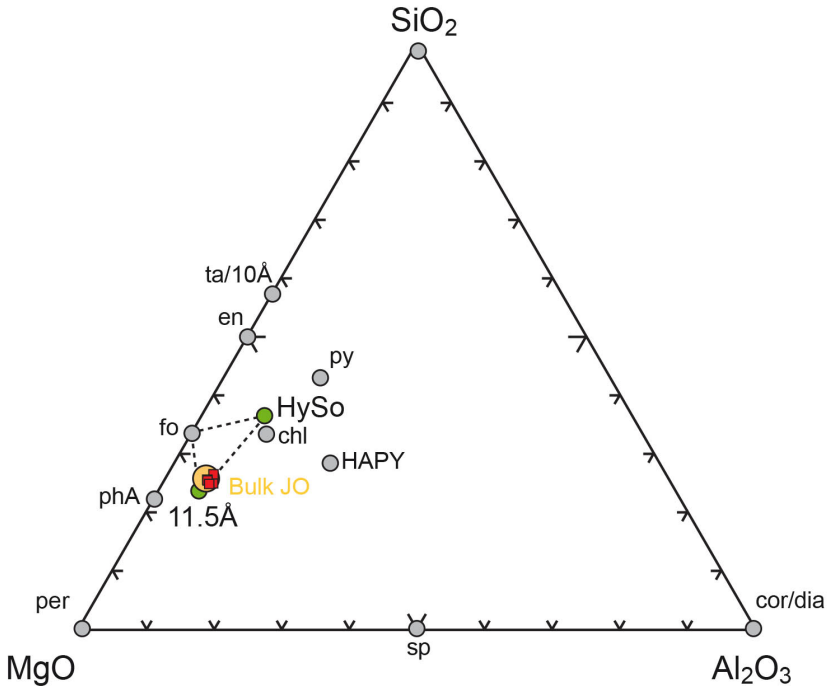

Figure S4 – Ternary diagram MgO-Al_2O_3-SiO_2 with H_2O in excess (MASH system). A selection of mineral phases is plotted in mol%, together with nominal composition of 11.5 Å phase and HySo. The experimental analysis are plotted as red squares. In yellow is plotted the bulk composition JO. Dashed lines represent coexisting phases at 6.5 GPa, 700°C.

S4. X-Ray powder diffraction analysis

X-ray powder diffraction

High-resolution and high pressure X-ray powder diffraction were performed at the ID09A beamline at the European Synchrotron Radiation Facility, ESRF (Grenoble, France). Representative X-ray powder pattern are reported in figures S5-S8. Table S6 summarize the crystallographic details (lattice parameters) of the 11.5 A and HySo phase, and the quantitative estimation (by Rietveld method) of the phases present in the analysed samples.

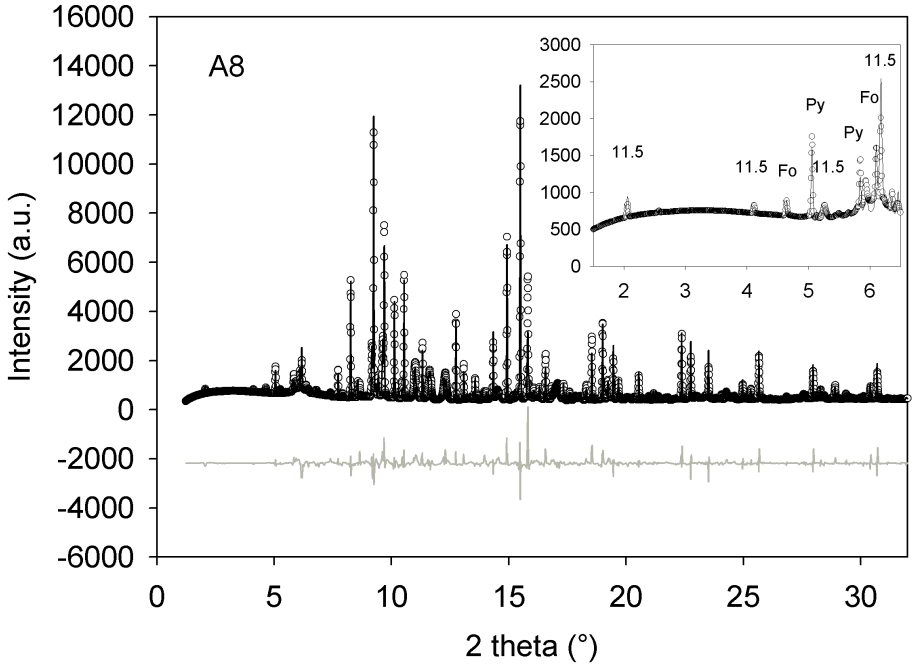

Figure S5

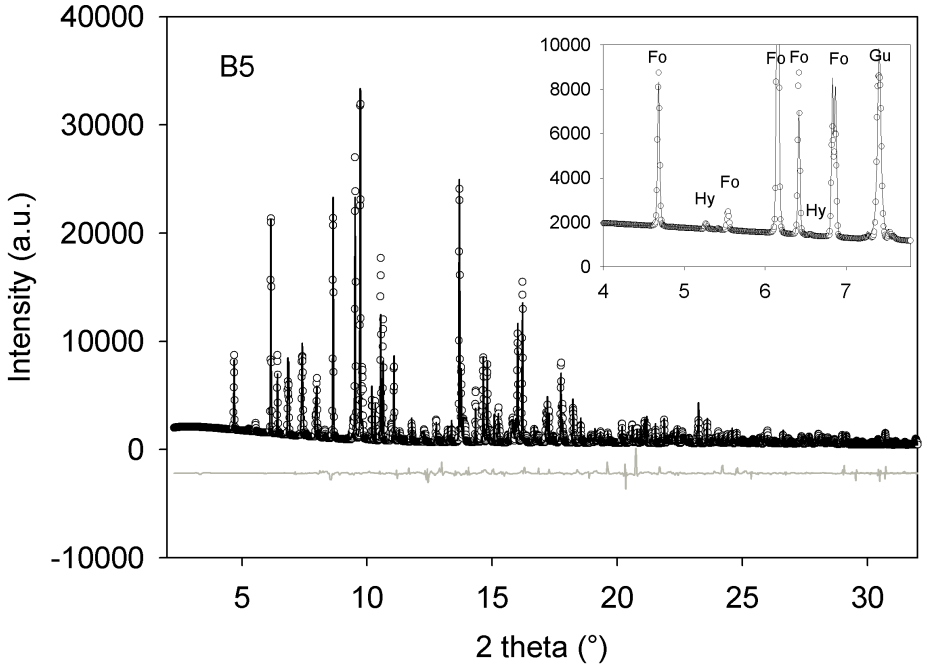

Figure S6

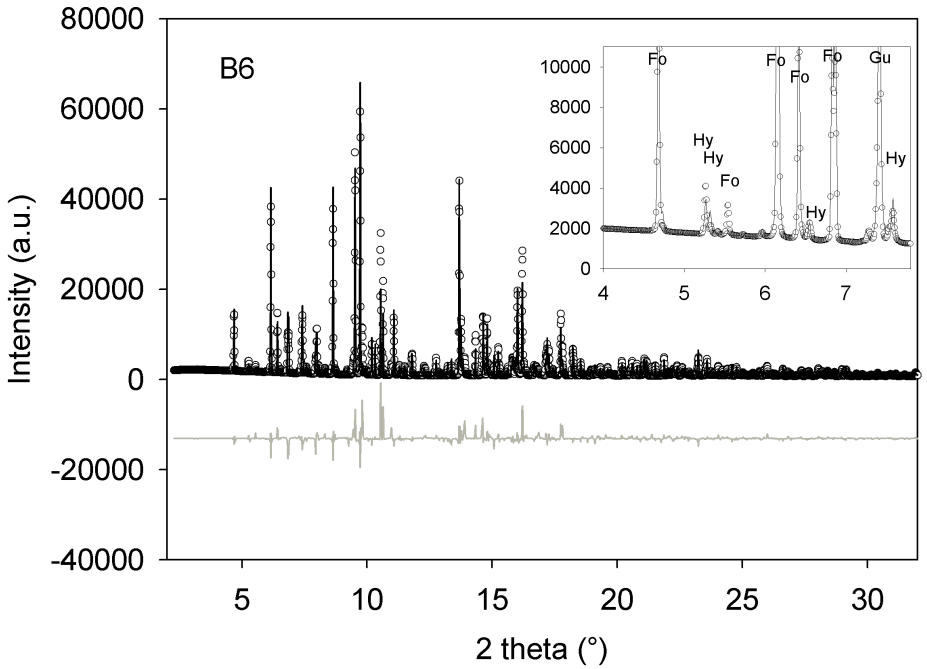

Figure S7

Figure S5-S7 Rietveld analysis of the sample A8, B4, B5 (circles: observed intensities; black line: Rietveld fit; gray line: difference curve). In the inset a portion of the low angle powder pattern is plotted and the diffraction peaks are labelled (11.5: 11.5 Å phase; Fo: forsterite; Py: pyrope; Hy: HySo; Gu: Guyanaite)

Sample	Fo	Py	Cen	11.5 Å	HySo	Gu
A8	8.0 wt %	61.0 wt %		30.6 wt % a = 9.0112(8) Å b = 5.2024(5) Å c = 23.220(17) Å β = 97.833(7)° V =1078.44(9) Å^3		0.4 wt %
B5	88.6 wt %		2.2 wt %		2.6 wt % a = 9.113(3) Å b = 14.743(5) Å c = 5.093(1) Å β = 98.53(2)° V = 676.7(2) Å^3	6.6 wt %
B6	83.5 wt %		0.8 wt %		10.3 wt % a = 9.135(1) Å b = 14.750(3) Å c = 5.0813(9) Å β = 98.40(1)° V = 677.3(1) Å^3	5.4 wt %
JO1	1.0 wt %			76.9 wt % a = 9.0115(5) Å b =5.2004(2) Å c =23.2039(8) Å β =97.858(5) ° V =1077.20(6) Å^3	22.1 wt % a =9.1508(4) Å b = 14.7428(8) Å c = 5.0710(3) Å β =98.300(4)° V =676.95(4) Å^3	

Table S6 – Mass fraction of crystal phases in the experimental runs as determined by Rietveld analysis. For the phases 11.5 Å and HySo, the lattice parameters are also reported. In the B5 and B6 samples the the olivine weight fraction can be overestimated, since it crystallized in large grains. The other phases were fine grained and their proportion is sensible.

High-pressure behavior

An example of high-pressure X-ray powder diffraction pattern at high pressure is reported in figure S8. The refined lattice parameters for the 11.5 Å and HySo phases were used for compressibility determination. Figure S9 and S10 report the volume and axial compressibilities for the 11.5 Å and HySo phases. The bulk modulus, obtained using a 2nd order Birch-Murnaghan EoS with K'=4, is respectively K_0=108.3(8) GPa and K_0=120.6(6) GPa. The 11.5 Å presents a slightly anisotropic compressibility, with the c axis, perpendicular to the layer staking, being the most compressible direction. However, the anisotropy is not pronounced and is negligible if compared with other hydrous phases like chlorite, talc, 10 Å and phlogopite. A direct comparison is reported in figure S11.

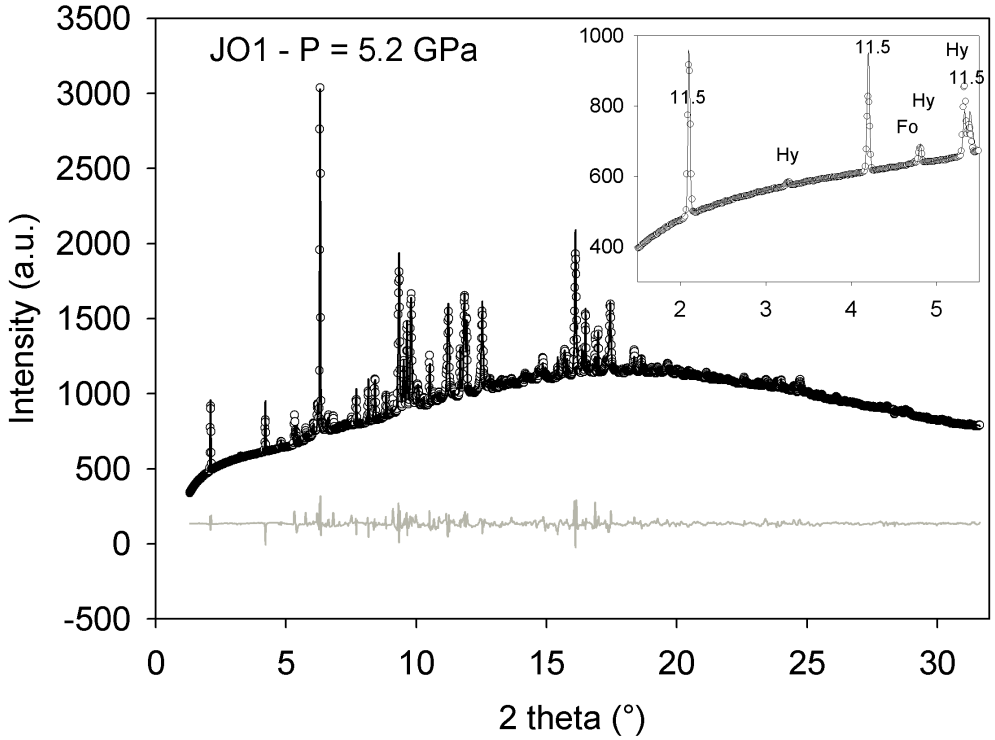

Figure S8 – X-ray powder pattern of the sample JO1 at 5.2 GPa. The experimental points are marked by empty circles; the calculated and profile difference curve by Rietveld fit are plotted with continuous line. The inset is an enlarged view of the low angle region, with the diffraction peaks labeled as in the previous figures.

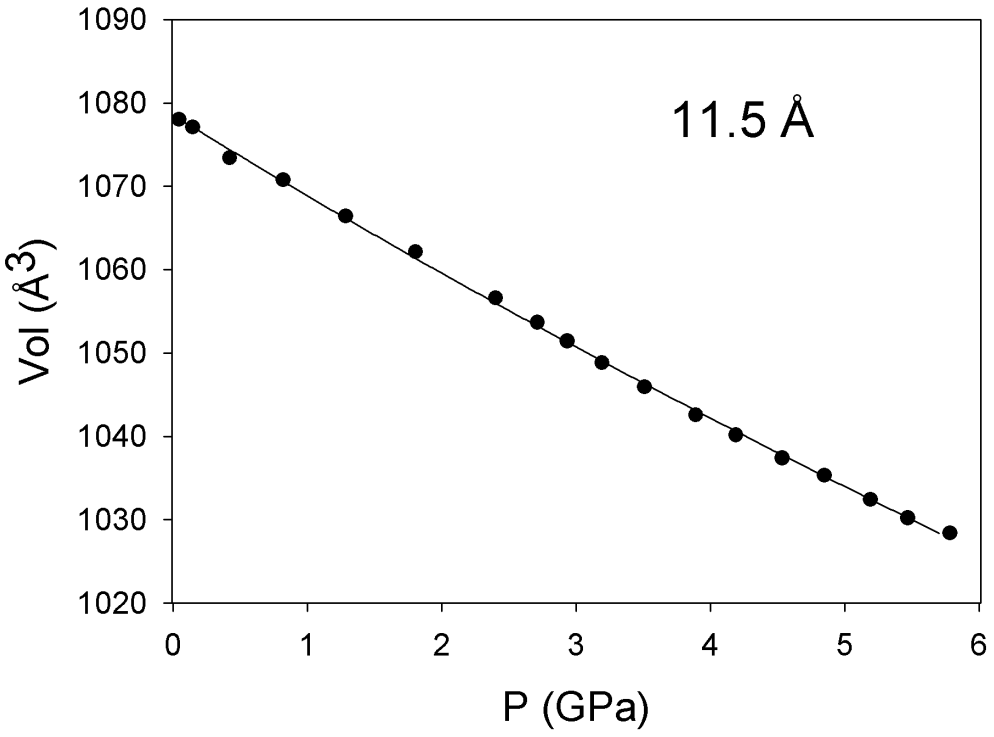

Figure S9 – Volume data at variable pressures for the 11.5 Å phase and fit of the experimental data with 2nd order Birch- Murnaghan equation of state.

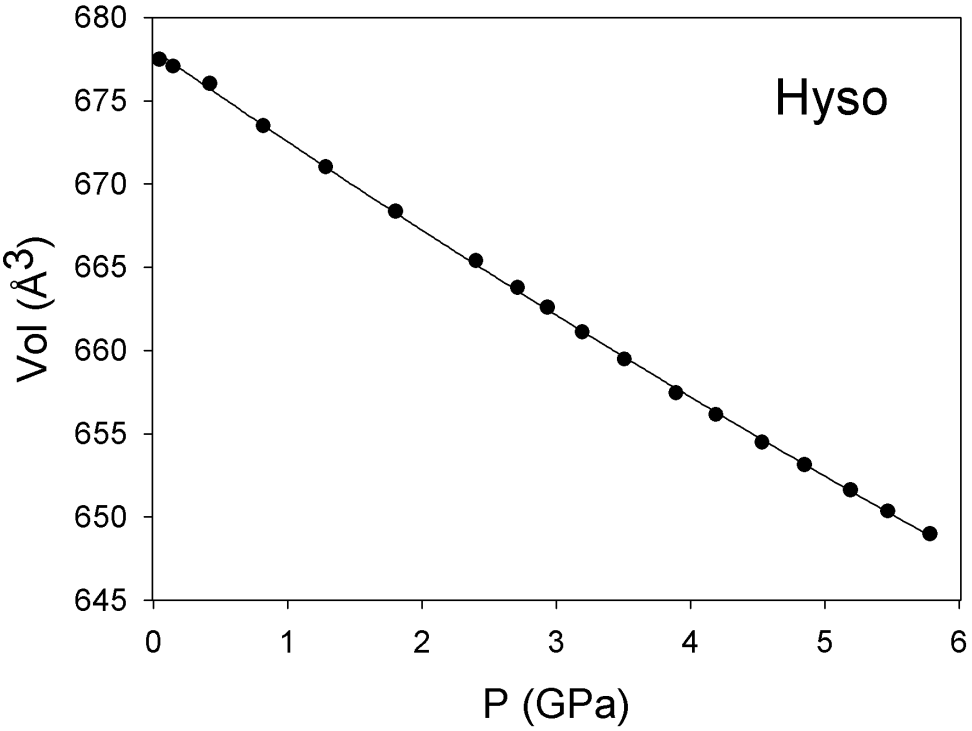

Figure S10 – Volume data at variable pressures for the HySo phase and fit of the experimental data with 2nd order Birch-Murnaghan equation of state.

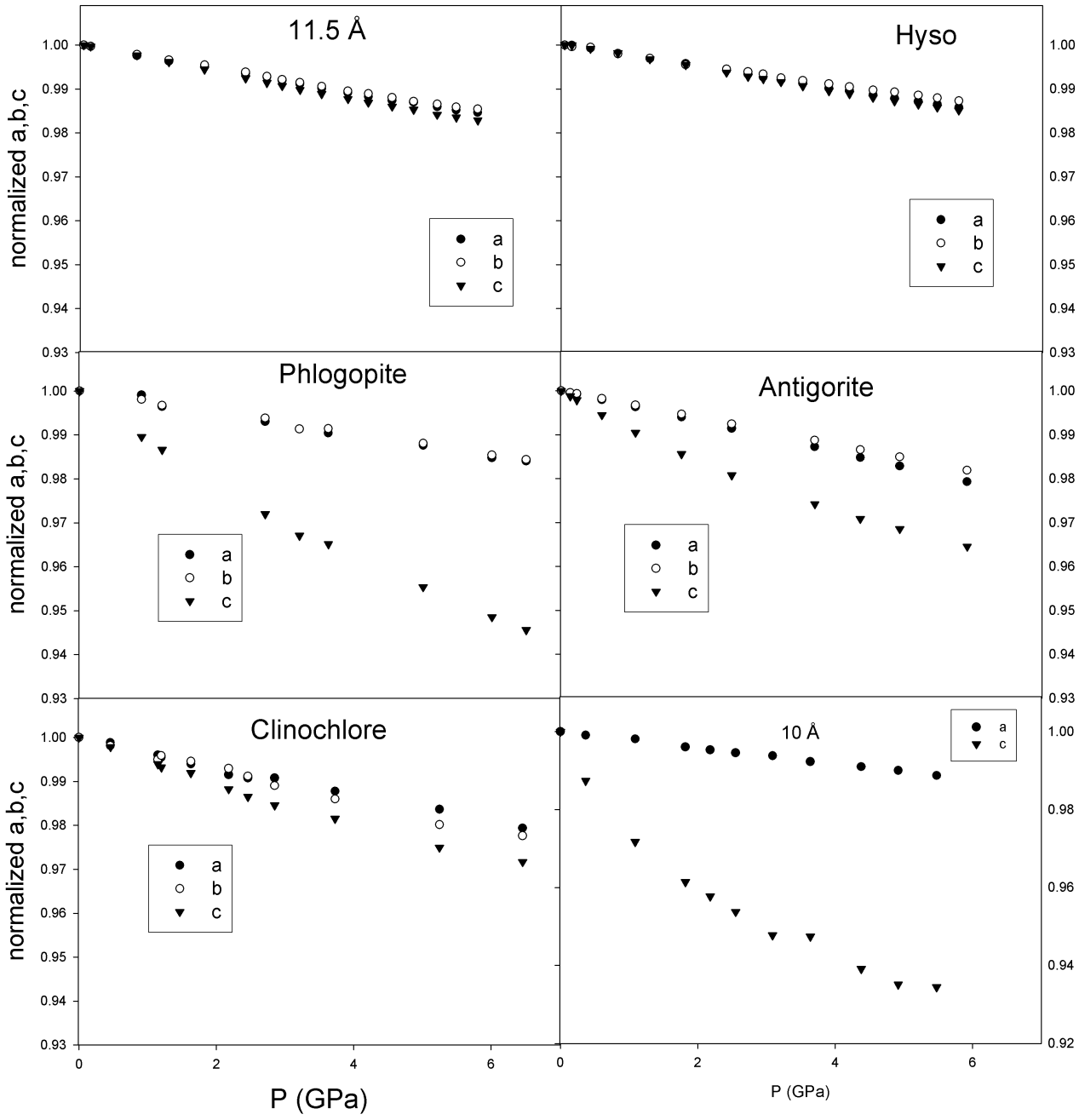

Figure S11 - Normalized axial compressibility of the 11.5 Å and HySo phase, and comparison with selected examples. The pressure scale and the normalized parameters scale are equal for all the plots for a direct comparison. The literature data are taken from: phlogopite, Comodi et al., 2004; clinochlore, Welch et al., 2001; antigorite, Nestola et al., 2010; 10 Å phase, Pawley et al., 2010

References

Christensen, N., Hansen, P., and Lehmann, M. S. (1976) Isotope effects in the bonds of beta-CrOOH and beta-CrOOD . Journal of Solid State Chemistry, 19, 299-304.

Fisher, G. W., Medaris, L. G. (1969) Cell dimensions and x-ray determinative curve for synthetic Mg-Fe olivines. American Mineralogist, 54, 741-753.

Fumagalli, F., Poli, S., Fischer, J. K., Merlini, M. and Gemmi, M. (2014) The high-pressure stability of chlorite and other hydrates in subduction melanges: experiments in the system Cr_2O_3-MgO-Al_2O_3-SiO_2-H_2O. Contribution to Mineralogy and Petrology, 167, 979.

Nestola, F., Ross, J. A., Zhao, J., Garrido, C. J., Sánchez-Vizcaíno, V. L., Capitani G., and Mellini, M. (2010) Antigorite equation of state and anomalous softening at 6 GPa: an in situ single-crystal X-ray diffraction study. Contribution to Mineralogy and Petrology 160, 33-43.

Pavese, A., Artioli, G., and Prencipe, M. (1995) X-ray single-crystal diffraction study of pyrope in the temperature range 30 - 973 K. American Mineralogist, 80, 457-464.

Pawley, A. R., Welch, M. D., Lennie, A. R., and Jones, R. L. (2010) Volume behavior of the 10 Å phase at high pressures and temperatures, with implication of H_2O content. American Mineralogist, 95, 1671-1678.

Ross, N.L. (1997) The equation of state and high-pressure behavior of magnesite. American Mineralogist, 82, 682–688.

Welch, M. D., and Marshall, W. G., (2001) High-pressure behavior of clinochlore. American Mineralogist, 86, 1380-1386.